

VLA Radio Observations of Blazar TXS 0506+056 Following an Astrophysical Neutrino Detection

DALTON J. RONAN,¹ GREGORY SIVAKOFF,² AND ALEXANDRA TETARENKO²

¹1401037

²Project Supervisor

Phys 499 - Final Report

ABSTRACT

Blazars represent an ideal candidate for the study of jet physics. They are observed throughout the electromagnetic spectrum (Radio to Gamma) and are believed to be sources for high energy gamma and cosmic rays. Extremely high energy (EHE) astrophysical neutrinos are believed to be associated with the generation of these gamma rays, and ultra high-energy cosmic rays (UHECRs). The blazar TXS 0506+056 was associated at a 3σ level as the counterpart to a recent IceCube neutrino detection. VLA radio observations of the blazar were taken over 7 epochs, from 2017 October 05 to 2018 March 04, to study the evolution of the jet's spectrum, and determine if a connection between the generation of the three phenomena exists. Spectral energy distributions (SEDs) for each epoch were resolved to a bandwidth of $\Delta\nu = 32$ MHz, and light curves were resolved down to every 10 seconds of observation time. The resulting figures were analyzed and compared to various models of jet emissions, and variability causes. SEDs match most closely to a single acceleration model with synchrotron and adiabatic losses accounted for. Light curves suggest the blazar was in an active state following the neutrino detection, although a clear connection between the events is not evident.

1. INTRODUCTION

Active Galactic Nuclei (AGN) represent a small portion of galaxies that have a highly luminous central region over some portion of the electromagnetic spectrum, believed to be powered by accretion of circumnuclear matter onto a central supermassive black hole. The energy released during this process may be converted into kinetic energy, in the form of a narrow outflow of relativistic plasma, called a jet (e.g. [Madejski & Sikora 2016](#); [Urry & Padovani 1995](#)).

Blazars are a particular case of active galactic nuclei associated with the relativistic jet emission being aligned (or nearly aligned) with the observational line of sight. Blazars can generally be separated into two categories based on their spectral features - more luminous flat spectrum radio quasars (FSRQs) with strong emission lines, and less luminous BL Lac objects with featureless spectra (e.g. [Böttcher 2010](#); [Mészáros 2017](#); [Urry 2012](#)). The relativistic flow of the head on jet causes the emission to be Doppler-boosted, leading the flux of the source dominated by the jet emission. This

makes blazars an ideal candidate for cosmic accelerators, and for the study of the origin of cosmic and gamma rays (Blandford & Königl 1979; Madejski & Sikora 2016; Marscher 2009; Mészáros 2017). Internal shocks close to the source of an astrophysical jet, as well as termination shocks extending further from the jet interacting with the intergalactic medium, are potential source locations for accelerating protons, generating ultra high-energy cosmic rays (UHECRs). Relativistic plasmas crossing these shocks are compressed, also accelerating electrons, generating gamma-rays through inverse-Compton scattering (synchrotron self-Compton models) (e.g. Böttcher 2010; Marscher 2014; Mészáros 2017; Pe’er & Casella 2009, are some recent reviews on jet emission models).

Observations across the electromagnetic spectrum can be used to study the properties of the jet, such as the shape and structure of the jet (e.g. Marscher 2009; Pe’er & Casella 2009). Blazar spectral energy distributions (SEDs) show they are sources dominated by non-thermal radiation emissions, with two major components: a low frequency (radio to UV) and high frequency (X-ray to γ -ray) (Fossati, et. al. 1998; Urry & Padovani 1995). At low (radio) frequencies, the spectrum is largely believed to be synchrotron emission of electrons interacting with the jets magnetic field (Gupta, Agarwal, & Bhagwan 2016). The shape of the radio spectrum of a jet can indicate the physical process occurring. Magnetic fields have been shown to have a nontrivial influence on the flux of blazars at radio wavelengths (Pe’er & Casella 2009).

Blazars are also known to exhibit variability on timescales of minutes to years at all frequencies. The cause of this variability is still under much debate, but some proposed processes include particle injection, acceleration and cooling (Ghisellini, Celotti & Costamante 2002), accretion disk base fluctuations propagating into jets, orbiting accretion disk hotspots, shocks in the jet changing outgoing flow (Gupta, Agarwal, & Bhagwan 2016), and “shock-in-jet” models, where shells of relativistic plasma are ejected at varying speeds, which collide and create shock fronts (Böttcher 2010). The shock-in-jet models reviewed by Böttcher (2010) agree with observed time lags between bands.

Astrophysical neutrinos have been believed to be associated with blazars (and thus the generation of UHECRs and gamma-rays) for some time now (e.g. Waxman & Bahcall 1998). Photohadronic and secondary nuclear production processes are the primary sources of astrophysical neutrinos (Murase, Inoue & Dermer 2014). When cosmic rays interact with the nearby photons or matter, EHE neutrinos can be produced (Dermer 2007; Mészáros 2017). Unlike high energy cosmic rays or γ -rays, neutrinos are a changeless and weakly interacting particle. As such, neutrinos are not affected by other charged particles, galactic or intergalactic magnetic fields, nor are they attenuated by interstellar or intergalactic dust, while cosmic rays and γ -rays may be. This makes these EHE astrophysical neutrinos an ideal candidate for the study of cosmic accelerators, and the origins of high-energy cosmic rays and cosmic-rays (Halzen 2016). FSRQs are the most likely bright neutrino sources (Atoyan, Dermer 2003). However, this potential has only recently been realized with the detection of extremely high energy (EHE) neutrinos by the IceCube Neutrino Observatory (e.g. IceCube Collaboration 2013).

An EHE astrophysical neutrino was detected by the IceCube Neutrino Observatory on 22 September 2017 20:54:30.43 UTC. Based on various X-ray observations of the determined emission region, the neutrino has been associated with blazar TXS 0506+056 at a 3.0σ confidence level (IceCube Collaboration 2018). The blazar was observed in the C and X radio bands over a series of observations

spanning from 05 October 2017, to 04 March 2017. Each observation was analyzed spectrally to study the evolution of the jets spectral index, and temporally to look for any structured variability in the flux density of the jet. The spectrum was resolved from $\sim 5 - 11$ GHz in 32 MHz bins, and the peak flux density was determined on 10 second intervals for each 11 minute observation.

2. DATA REDUCTION AND OBSERVATIONS

2.1. VLA Observations of TXS 0506+056

Following the IceCube detection of the EHE neutrino, the blazar TXS 0506+056 was observed over seven epochs (2017 October 05, 06, 09, 12, 24, 2017 November 21, and 2018 March 04) with the Karl G. Jansky Very Large Array (VLA). Each epoch of data consisted of approximately 11 minute on source observations in the C (4 - 8 GHz) and X (8 - 12 GHz) bands. Epochs one to six were completed in the VLA B configuration, while the seventh was in the A configuration. All X band observations used a 9 telescope arrangement, while the C band arrangement used 8, with exceptions on the third and fifth observations, which used 7, as antennas 8 and 15 lost data during observations. Weather conditions during observations were usually fair, with epoch two being the only exception, with observing conditions showing a noticeable negative effect on the data.

2.2. Editing and Flagging

Prior to imaging and analyzing the VLA data, each measurement set needed to be viewed and edited to remove any obvious errors in the visibility data, and then calibrated to determine the true visibility from the observed visibility. These processes were carried out with the Common Astronomy Software Application package (CASA ¹).

The initial step for each reduction was to perform some standard flagging routines on the measurement sets²). All flagging was completed using the `flagdata` command in CASA . This includes flagging all system configuration scans, flagging the first and last 3–4 channels for each spectral window, and performing a ‘quack’ flag. The purpose of ‘quacking’ the data is to remove data at scan boundaries, and account for the settle down time of the array. For all data sets, the beginning 3 seconds were flagged from each scan, as this was the integration time for all observations.

Further required flagging was found by viewing amplitude and frequencies of the source and calibrators versus observation times, spectral windows, frequency, and uv distance. It is to be expected that the phase and amplitude of the observed sources may change over the course of an observation, however any variability in these values throughout an observation should occur in a somewhat consistent manner, i.e. vary smoothly with time. Any visibility measurements in these plots that were inconsistent in this regard were flagged and removed from the measurement set.

Visibility data from C band observations had very little radio-frequency interference (RFI)³, and did not require a significant amount of additional flagging. Typically only a few channels from a few spectral windows were flagged for a small number baselines.

The X band observations regularly exhibited phase inconsistencies at a frequency of 11-11.2 GHz for antennas ‘ea05’ and ‘ea17’, so data from these antennas were flagged at these frequencies. One

¹ version 5.1; <https://casa.nrao.edu/>

² For more in-depth information on flagging procedures, see https://casa.nrao.edu/index.php/Karl_G._Jansky_VLA_Tutorials

³ Any radio signal that is within the observation frequency band that does not originate from the scientific target source, e.g. terrestrial based sources.

Source	Description
J0509+0541	Target source
3C138	Flux calibrator
3C147	Polarization Leakage
J0502+0609	Secondary Calibrator

Table 1. Sources observed, and their observing purpose, throughout all observations.

to two individual calibrator observations had significant amplitude spikes in spectral windows 13 (11,035 MHz), 14 (11,163 MHz), and 16 (11,419 MHz) during scans 8 and 10 for most observations. This is consistent with the frequency range that phase scattering was observed, suggesting some sort of interference could be present at that frequency.

2.3. Standard Calibration

Once the data was properly edited, the standard calibration process could be completed. Calibrating involves taking “uncalibrated” data, using `CASA tasks`⁴ to solve for calibration tables from the observations calibrator sources. The phase and amplitude corrections from the tables are then applied to the target source data, creating the “calibrated” data. The calibrator sources for these observations, and their uses are given in Table 1.

In some cases, antenna positions may need to be corrected. However, for our observations, no antenna position correction tables were available, so it was assumed the antenna positions were correct.

First, it is necessary to provide flux density values (in Janskys) to the measured amplitudes of the flux calibrator (3C138), by comparing the measured values to a model of the source. The flux calibrator was observed for approximately 4 minutes near the beginning of every observations, before the array began observing of the target source and secondary calibrator. The flux scale was set in `CASA` with the `set jy` command. The model used for all data epochs was taken from the “Perley-Butler 2013” standard.

The `CASA` task `gaincal` was then used to solve for the initial phase calibration for all three of the calibrator sources. For all calibration tasks, the `CASA` standard minimum signal-noise ratio of `minsnr = 5` was used throughout the entire reduction process. This restriction ensures solutions are at relatively high signal-to-noise ratios. Initial phase solutions were plotted with `plotcal` to inspect the solutions. In order for the corrections to be properly applied, they must be smoothly varying with time. All derived corrections at this stage were acceptable for all antennas, and no further flagging was required. An identical process was used to solve for antenna-based delay calibrations. In all cases, solutions were within an acceptable range of ± 2 ns.

With these initial calibrations completed, solving for the complex bandpass (the instrumental response as a function of frequency) can now be completed. By applying the previously derived phase solutions, bandpass solutions were determined with the `CASA` task `bandpass`. Plots were again inspected for flat or smoothly varying solutions. For the C band observations, some bandpass solutions showed a significant jump out of phase compared to solutions for adjacent channels. These

⁴ All `CASA` tasks will be displayed in this monospaced font.

Configuration	A	B
Frequency Band	Synthesized beamwidth	(arsecs)
C (6 GHz)	0.33''	1.0''
X (10 GHz)	0.20''	0.60''

Table 2. Synthesized beamwidth (in arcseconds) for the VLA C and X bands in A and B configurations. Taken from: <https://science.nrao.edu/facilities/vla/docs/manuals/oss/performance/resolution>

inconsistent channels were then flagged from the data set in order to ensure the calibration could be easily transferred to the other sources. Since the flux calibrator (3C138) was used to solve for the delay solutions in all cases, a “nearest” temporal interpolation was used when solving for the complex antenna gain corrections. Gain corrections were then appended to the calibration tables for each of the calibrator sources.

The final step in the standard calibration process was to use the flux calibrator to determine the flux density of the secondary calibrator (J0502+0609). While a model was used for the flux density of the primary calibrator (the `set jy` task), no such task was used for the secondary calibrators. So the flux scale of the primary calibrator was used to find the true flux density of J0502+0609 with the `fluxscale` task.

With all calibration solutions derived and checked, and all further flagging determined and completed, the calibration tables were applied to the data for each source using the `applycal` task. Before proceeding, the validity of previous calibrations was checked by plotting the new corrected phase and amplitude against each other. With a successfully calibrated data set, one would expect an oval shape of visibility points centred at zero phase and the previously determined amplitude. Some observations required minor additional flagging to clear up some of the scatter of visibility points around the ‘blob’.

2.4. Initial Imaging

The calibrated data sets for the C and X band were split off into two upper and lower base-bands for each epoch (5 GHz and 7 GHz for C, and 9 GHz and 11 GHz for X). An initial image of blazar was made in each base-band using the `clean` task in order to check for any obvious errors from poor calibration or missed data flagging. This task uses some form of the CLEAN algorithm to perform a deconvolution of the dirty image. The algorithm assumes the dirty image consists of point sources, and finds the peak sources. It then multiplies this point source by some gain factor (≤ 1) and subtracts this point convolved with the dirty beam (or “point spread function” [psf]). This process is repeated until a predefined number of iterations has been completed, or the next peak is below a minimum threshold value. The subtracted “CLEAN” components are stored, and re-convolved with an idealized, 2D Gaussian “clean” beam. The resulting CLEAN image is an accurate model of the true sky visibility. Some key parameters used for this initial imaging are:

- `niter = 5000` - maximum number of iterations per CLEAN cycle before process stops
- `mode=mfs` - multi-frequency synthesis imaging
- `gain=0.1` - amount peak is multiplied by before subtraction
- `threshold=1.0mJy` - minimum flux density a component before process stops

- psfmode=Clark - FFT⁵ based CLEAN algorithm, [Clark \(1980\)](#)
- weighting=natural - weighting of uv cells applied to sampling function

The weighting function $W(u, v)$ is applied to the sampling function to weight uv cells. A natural weighting effectively weighs occupied uv cells by the inverse of the the noise variance σ^2 , and gives zero weight everywhere else:

$$W_N(u, v) = \frac{1}{\sigma^2} \quad (1)$$

Natural weighting maximizes point source sensitivity, with the lowest rms noise in the resulting image ([CASA 2010](#)), making it a natural choice for observing TXS 0506+056, as it is essentially a point source.

Cell sizes (pixel sizes) and image size also need to be specified. A standard practice to determine the cell size is to fit 5~7 pixels across the synthesized beam. The synthesized beam sizes for the different bands and configurations are provided in Table 2. Thus for epochs one to six, the C and X band cell sizes were 0.15'' and 0.01'' respectively, and for epoch seven they were 0.05'' and 0.03'' respectively. The total image size is determined from the Rayleigh criterion

$$\theta = 1.22 \frac{\lambda}{D}, \quad (2)$$

where θ is the angular resolution, λ is the wavelength, and D is the VLA antenna diameter, which is 25 meters. In order to maximize the efficiency of the CLEAN algorithm, the image size is selected to be the nearest power of 2 of the angular resolution of the array at the observing frequency, i.e.

$$\text{Image size} = 2^n \simeq \theta. \quad (3)$$

For epochs one to six, an image size of 4096 was chosen for both bands, and 8192 was chosen for the bands in the seventh epoch.

2.5. Self-Calibration

After the initial imaging, each data set underwent the process of self-calibration. This involves using an model of the target source itself to determine calibration corrections rather than using calibrator sources. For these observations, only a phase self-calibration was completed. An initial shallow CLEAN (200 mJy threshold) of the calibrated data was completed to build the initial self-cal model. Phase solutions were then determined at an interval of thirty seconds, and checked for smoothly varying solutions, and then applied to the visibilities to create the self-calibrated image. This process was repeated, performing a slightly deeper clean and solving on shorter intervals each iteration, until an improvement in rms noise in the local area near the source was not seen. In all cases, the final self-calibration solutions were at a three second interval (the integration time), and the image was CLEAN'ed down to threshold of 1 mJy.

Self-calibration resulted in an improvement of rms noise from ~ 10 mJy in the initial CLEAN images, down to a sub-mJy level. A significant change in amplitude was seen in the epoch 2 images.

⁵ Fast Fourier Transform – discrete Fourier transform algorithm that requires interpolating data onto rectangular grid.

base-band	epoch 1	epoch 2	epoch 3	epoch 4	epoch 5	epoch 6	epoch 7
5 GHz	565.9 ± 0.5	586.9 ± 0.3	563.5 ± 0.7	571.9 ± 0.3	608.0 ± 0.9	696.2 ± 0.5	667.2 ± 0.5
7 GHz	625.6 ± 0.7	634.9 ± 0.8	623.5 ± 0.9	629.1 ± 0.6	698.1 ± 0.9	668.4 ± 0.6	704.5 ± 0.4
9 GHz	664.0 ± 0.4	660.2 ± 0.5	649.6 ± 0.5	661.8 ± 0.4	723.8 ± 0.4	666.2 ± 0.5	731.1 ± 0.6
11 GHz	697.0 ± 0.5	719.8 ± 0.5	670.1 ± 0.4	722.5 ± 0.3	752.3 ± 0.4	645.6 ± 0.4	786.4 ± 0.6

Table 3. Flux densities (mJy) of TXS 0506+056 after self-calibration. Final images were CLEAN'ed to a 1 mJy threshold, and phase solutions were determined down to the integration time (3 seconds).

The initial clean image for this epoch had a much lower flux density due to a phase decorrelation caused by poor weather conditions during the observation. The final self-calibrated flux densities (in mJy) are given in Table 3. The uncertainties in these values were determined by finding the mean rms noise of the CLEAN image in an annular region of radii 50 - 60 pixels centred around the target source. A first look at the blazar's SED and light curve based on these values are shown in Figure 1.

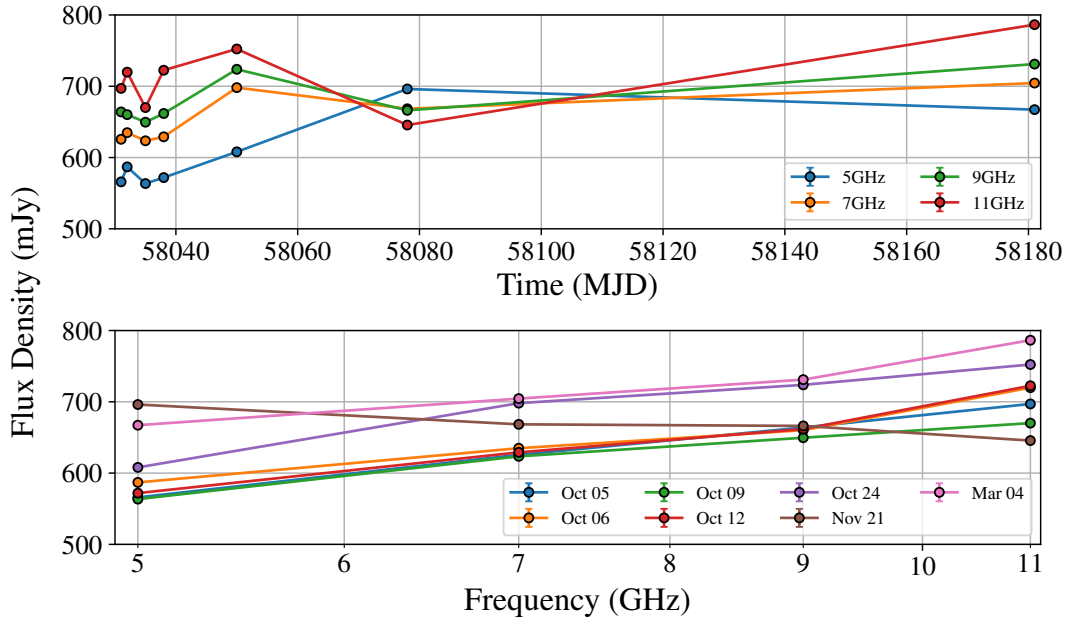


Figure 1. (Top) Flux density (mJy) vs. time of TXS 0506+056 for 7 observation epochs. (Bottom) Spectral energy distribution (SED) from 5 GHz to 11 GHz for 7 observation epochs. Solid lines do not represent any data fitting, and are included for ease of visualization of the trends.

3. RESULTS

Figure 1 displays both the flux density as a function of time (*top*) and frequency (*bottom*) of TXS 0506+056 for the 7 epochs, imaged over the entire ~ 11 minute observation. Referring to the top figure, we can see a trend of decreasing flux density in the 7, 9 and 11 GHz base-bands between epochs 5 and 6, while the 5 GHz exhibits a steady increase over this period. A sharp amplitude decrease is visible in the 11 GHz base-band from epoch 2 to 3.

The bottom figure shows the SED of TXS 0506+056, where we observe a general trend of increasing flux density with frequency. This spectrum is typical of non-thermal emission from a compact jet (e.g. [Biermann & Strittmatter 1987](#)). An exception is seen for epoch 6 (2017 November 21),

base-band	epoch 1	epoch 2	epoch 3	epoch 4	epoch 5	epoch 6	epoch 7
5 GHz ($\nu_0 = 5.3$ GHz)	0.14 ± 0.01	0.13 ± 0.01	0.25 ± 0.01	0.15 ± 0.01	0.36 ± 0.01	0.02 ± 0.01	0.04 ± 0.02
7 GHz ($\nu_0 = 7.5$ GHz)	0.41 ± 0.01	0.47 ± 0.01	0.33 ± 0.02	0.36 ± 0.01	0.44 ± 0.01	-0.12 ± 0.01	0.04 ± 0.02
9 GHz ($\nu_0 = 8.5$ GHz)	0.33 ± 0.02	0.43 ± 0.02	0.21 ± 0.01	0.33 ± 0.01	0.13 ± 0.01	-0.08 ± 0.02	0.34 ± 0.02
11 GHz ($\nu_0 = 11$ GHz)	-0.05 ± 0.02	0.18 ± 0.02	0.19 ± 0.01	0.28 ± 0.01	0.08 ± 0.02	-0.06 ± 0.02	0.24 ± 0.03

Table 4. Results of spectral index fitting and the reference frequency used for each base-band.

where the relation is inverted, and we observe flux density decreasing with increasing frequency. A steeper increase in flux between 5 GHz and 7 GHz is observed on 2017 October 24 (epoch 6), and between 9 GHz and 11GHz on 2018 March 04 (epoch 7).

3.1. Spectral Analysis of TXS 050+056

3.1.1. Spectral Index

The spectral index, α , is a measurement of the relation between the flux density of a source and the frequency. This relation is often written as

$$S_\nu = A \left(\frac{\nu}{\nu_0} \right)^\alpha, \quad (4)$$

where S_ν is the flux density, A is some amplitude, and ν_0 is a reference frequency. The spectral index of a source can thus be calculated by performing a linear fit on the log of the flux density versus the log of the frequency.

In order to examine to the evolution of TXS 0506+056's spectrum in greater detail, the spectral resolution of the SED was increased for each observation. Each base-band consists of eight spectral windows, each of which are comprised of 64 channels with a of bandwidth $\Delta\nu = 2000$ kHz, for a total spectral window bandwidth of $\Delta\nu = 128$ MHz. The self-calibrated data sets were partitioned into 32 sub-bands of $\Delta\nu = 32$ MHz, dividing each spectral window into four sub-bands (16 channels per sub-band). Each sub-band was again CLEAN'ed and imaged in CASA using the same parameters as during the initial and self-calibration steps, and the flux densities and rms errors were determined to create a high-spatial resolution SED for each epoch.

The spectral index (see sec.3.1.1) for each spectral window was determined by performing a Bayesian linear regression to fit the data according to Eq. 4, where the reference frequency ν_0 was chosen to be the frequency at the centre of the sub-band. The results of the spectral index fitting are given in Table 4.

The resolved spectral energy distributions for each epoch are displayed in Figure 2, (a) – (g), with the index value for each base-band displayed on the plot. The lower panel shows the residuals of the observed flux densities compared to the power law model described by Eq. 4. The residual R_i for

each data point was determined by the formula

$$R_i = \frac{S_i - S_{i,\text{model}}}{\delta S_i}, \quad (5)$$

where S_i and δS_i are the observed flux density and the rms error associated with it respectively, and $S_{i,\text{model}}$ is the expected flux density from the power law model. The red dot-dash line does not represent any fit to the data, and is included to guide the eye to the general trend of the SED.

The general behaviour of the SEDs is an initial flat spectral slope, increasing through the intermediate base-bands, and shallowing out at 11 GHz. The opposite structure is seen in epoch 6 (Figure 2,(f)), where a negative spectral index is observed. The residuals show significant deviation from the power law model. Interpretations and implications of these results will be discussed in section 4.2.

3.2. Variability of TXS 0506+056

The temporal variability of TXS 0506+056 was analyzed in order to look for any variability over observations to indicate any potential flares, or structural changes occurring to the jet. The target source was observed for approximately 11 minutes each epoch, with the array shifting to observe the secondary calibrator at around the 5–6 minute mark. The total 11 minute scan was divided into 71 time bins, giving the light curve a temporal resolution of 10 seconds. The source was deconvolved and imaged on each time bin to track the variability in the flux density.

To quantify the temporal variability of the source, a variability test was performed on each resolved light curve. The weighted mean flux density was calculated for the entire observation. A chi-squared test was then performed on the resolved temporal data (S_i), comparing it to a model with a constant flux density ($S_{i,\text{mean}}$) at the weighted mean value, i.e.

$$\chi_i^2 = \sum \frac{(S_i - S_{i,\text{mean}})^2}{S_{i,\text{mean}}} \quad (6)$$

The χ^2 values, degrees of freedom (DOF), the log of the null hypothesis probability, and percent rms for each base-band are given in Table 5. The beginning scans (at 0 and ~ 6 minutes after the start of the observation) were consistently multiple σ lower or higher than both the weighted mean flux density for the observation, and the next point in the sequence. This is likely a result of the array changing from other sources shortly before the target observations, and the time bin being too short to allow for the array to fully settle down on target. These data were removed from the analysis procedure, resulting the DOF varying between 62-64. Large χ^2 values (> 50) indicate a poor fit to a constant flux density model, suggesting statistically significant variability in the blazar emission (or perhaps a steady increasing/decreasing flux density at the very least). The ‘%’ rms was calculated as

$$\% \text{rms} = \sqrt{\frac{\sigma_{\text{XS}}}{S_{i,\text{mean}}}} \times 100, \quad (7)$$

where σ_{XS} is the excess variance, defined as

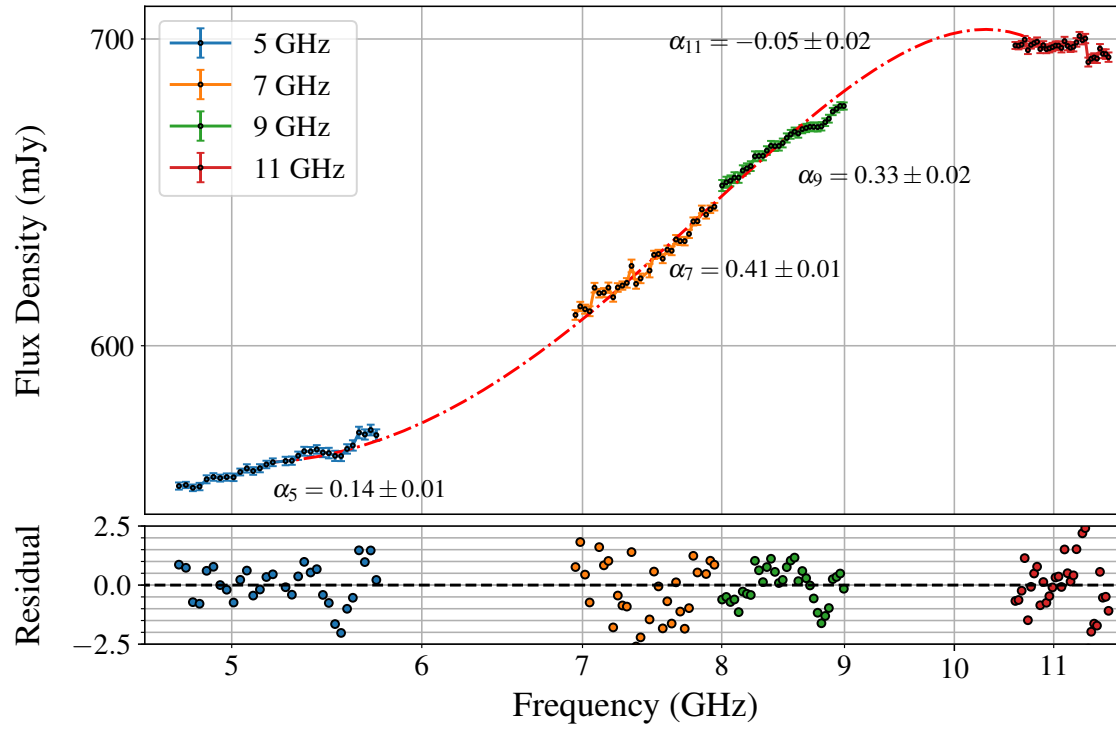
$$\sigma_{\text{XS}} = \sigma_{\text{flux}} - \bar{\sigma}_{\text{rms}}, \quad (8)$$

		χ^2 total	DOF	log(nhp)	% rms
epoch 1	5 GHz	78.8	63	-2.45	0.0443
	7 GHz	128.82	64	-12.75	0.148
	9 GHz	10.76	63	0	...
	11 GHz	46.74	63	-6.40×10^{-2}	...
epoch 2	5 GHz	542.37	64	...	0.349
	7 GHz	605.34	62	...	0.665
	9 GHz	390.7	64	...	0.649
	11 GHz	1030	64	...	1.09
epoch 3	5 GHz	12.02	63	0	...
	7 GHz	13.8	64	0	...
	9 GHz	15.24	62	0	...
	11 GHz	32.36	62	-1.00×10^{-3}	...
epoch 4	5 GHz	21.19	64	0	...
	7 GHz	6.49	63	0	...
	9 GHz	27.2	64	0	...
	11 GHz	129	63	-13.24	0.161
epoch 5	5 GHz	15.93	64	0	...
	7 GHz	21.97	63	0	...
	9 GHz	9.91	64	0	...
	11 GHz	33.38	64	-1.00×10^{-3}	...
epoch 6	5 GHz	20.87	64	0	...
	7 GHz	47.31	64	-6.08×10^{-2}	...
	9 GHz	15.58	63	0	...
	11 GHz	716.44	63	0	...
epoch 7	5 GHz	92.28	63	-4.65	0.121
	7 GHz	2780	64	...	1.85
	9 GHz	484.7	63	...	0.290
	11 GHz	446.6	63	...	0.493

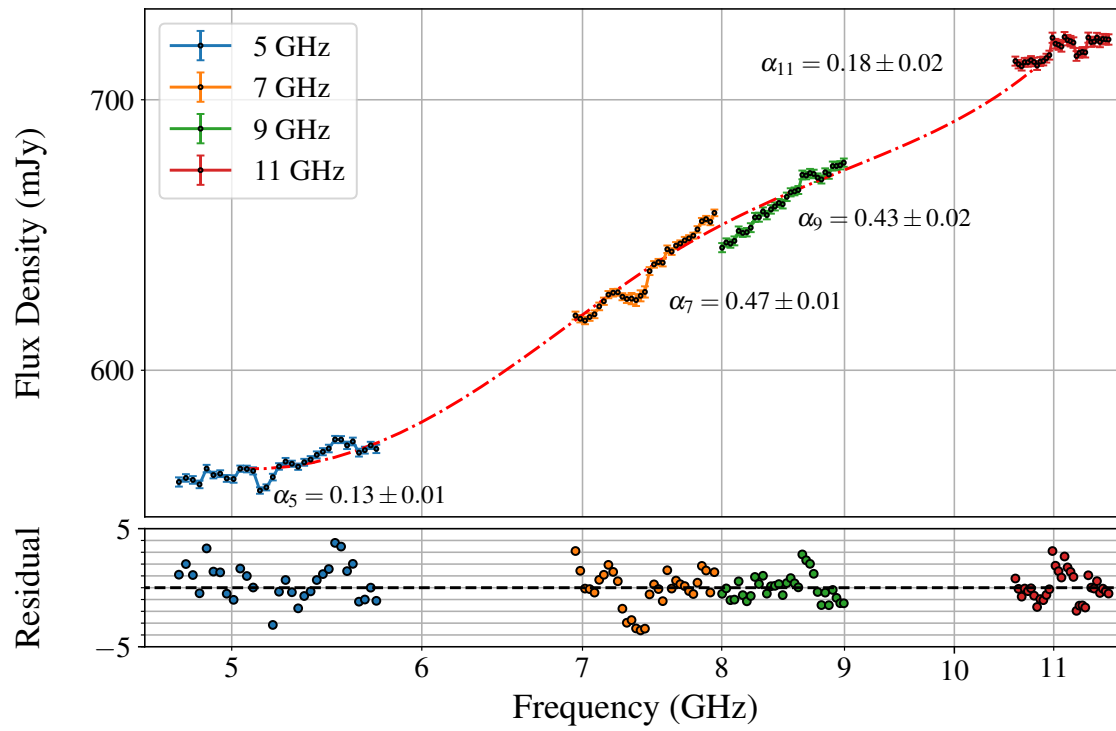
Table 5. Results of variability metrics for each observation base-band. Ellipsis in column 3 represent a zero null hypothesis probability ($\log(0)$). Highlighted rows are results which show statistically significant variability.

where σ_{flux} is the variance of the flux density, and $\bar{\sigma}_{rms}$ is the average rms noise of the entire observation. Not applicable values in the ‘% rms’ column are indicative of non-significant variability, i.e. variability of the source was much less than the uncertainties of the measured rms, while values of $\sim 0.1\%$ indicate potential variability. These two parameters are the best indicators of the variability of the source⁶. Epochs that reported positive variability results are highlighted in Table 5, and their resolved light curves are shown in Figures 3–8. The variability results will be discussed in further detail in section 4.3.

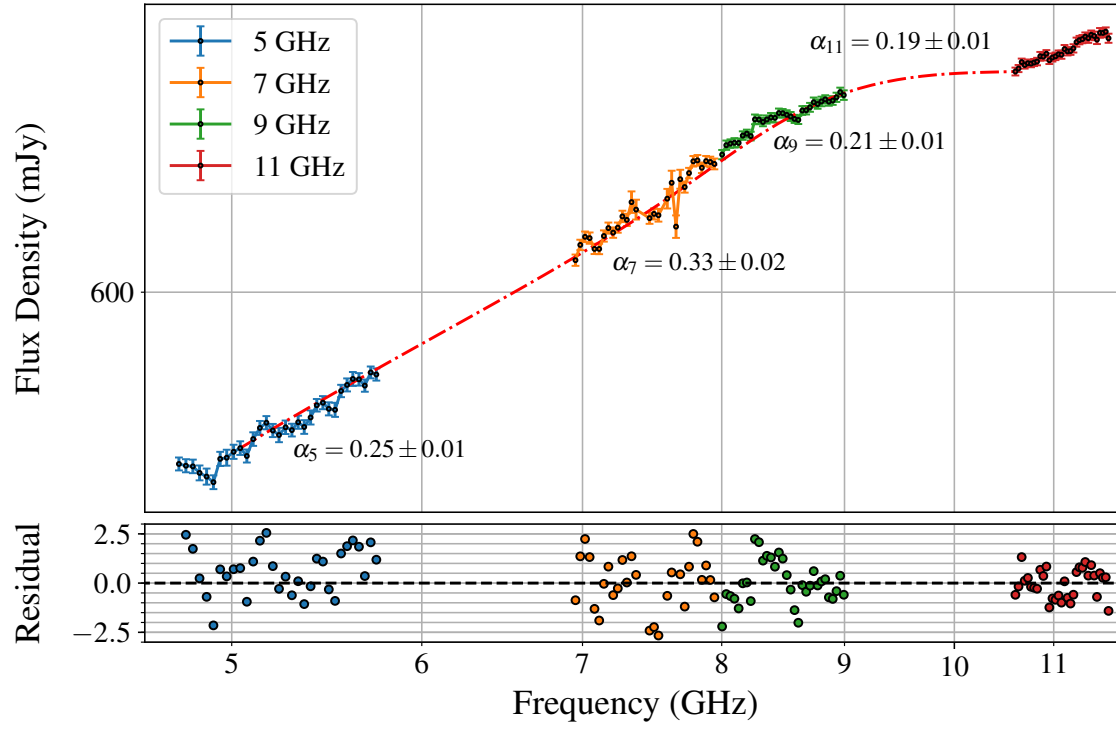
⁶ The null hypothesis probability (column 3) shows inconsistent results in terms of variability.



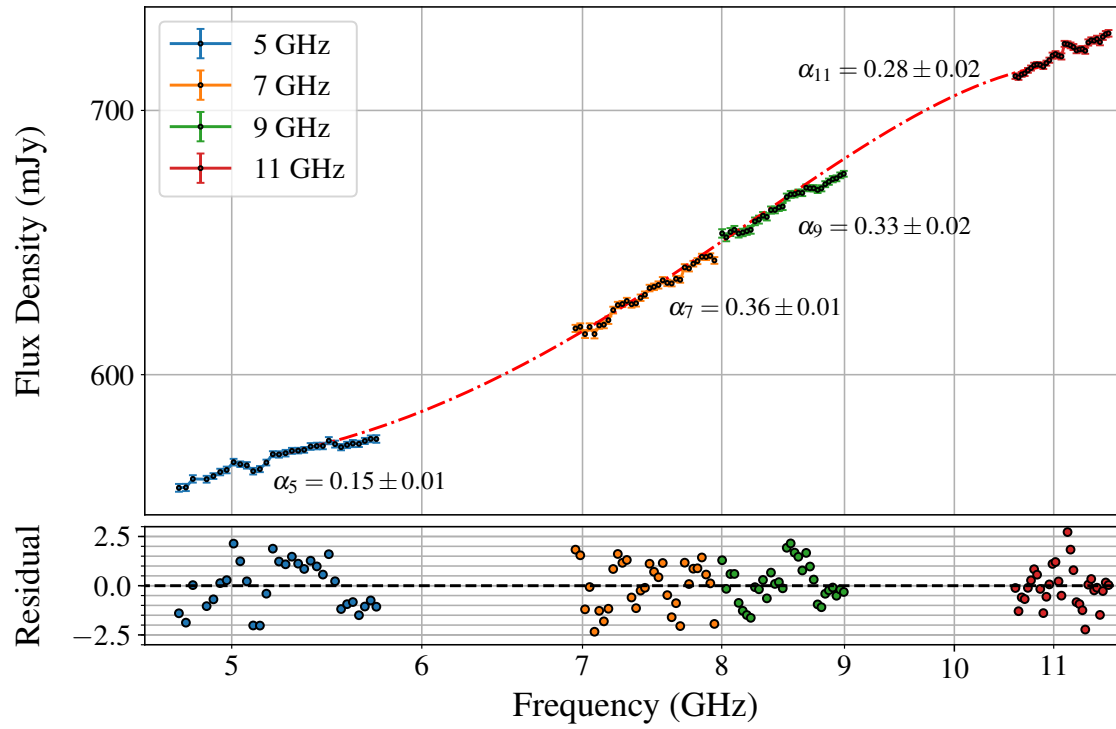
(a)



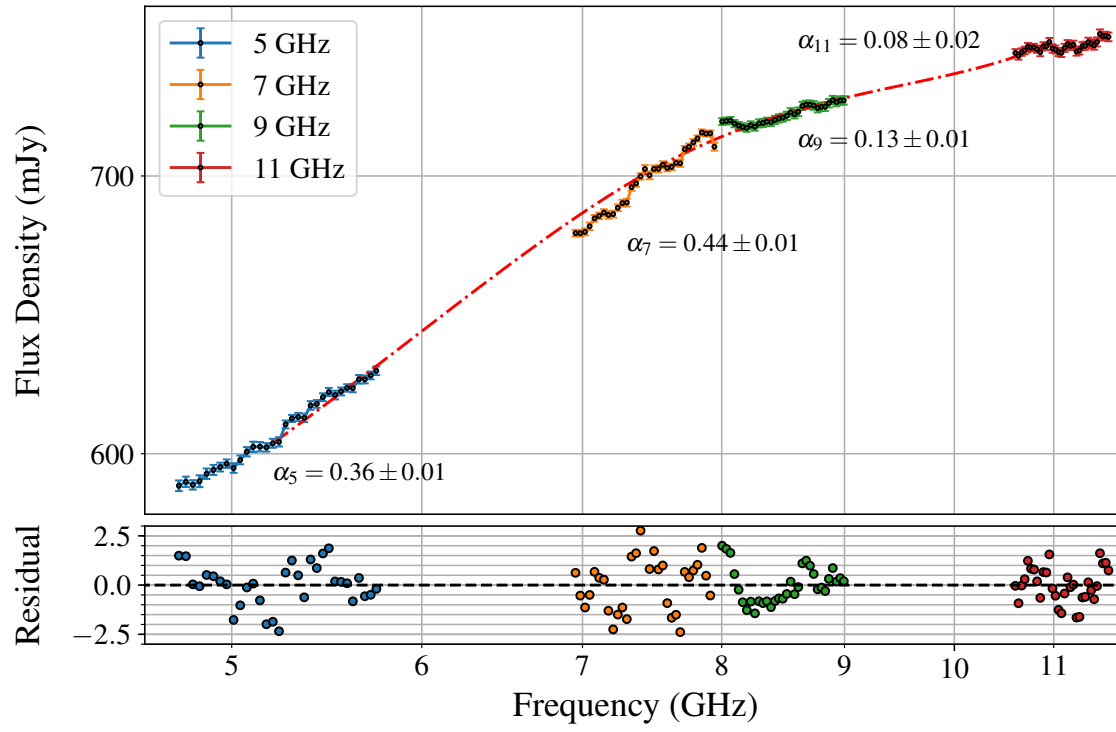
(b)



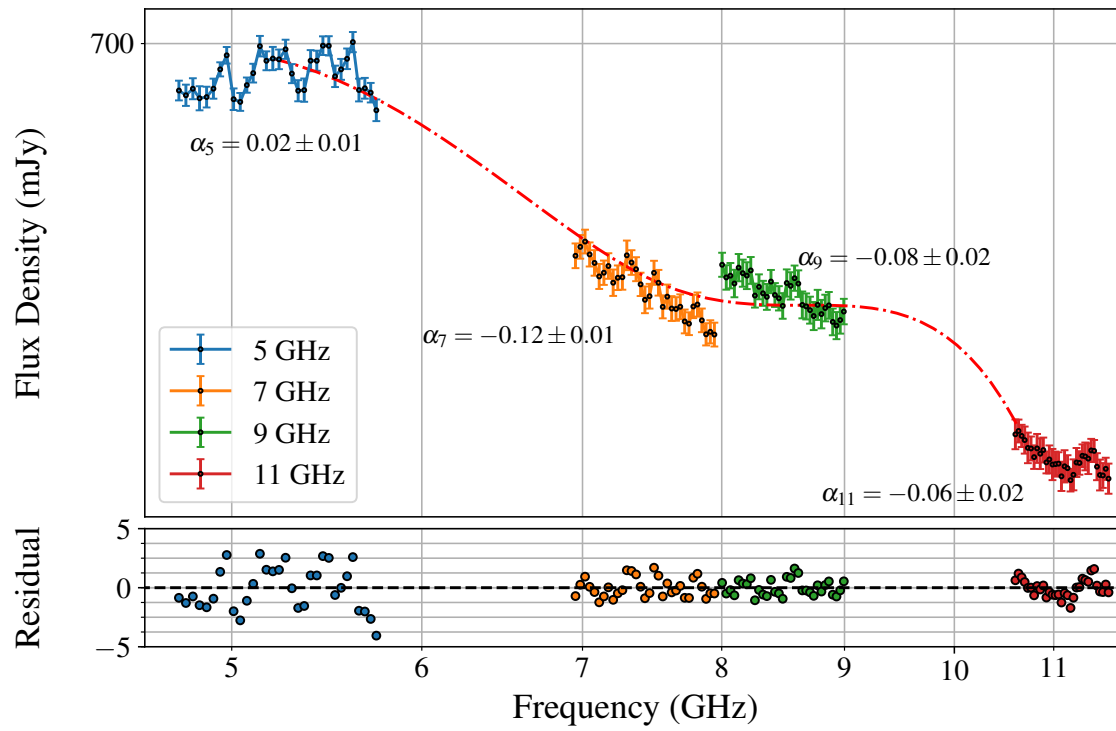
(c)



(d)



(e)



(f)

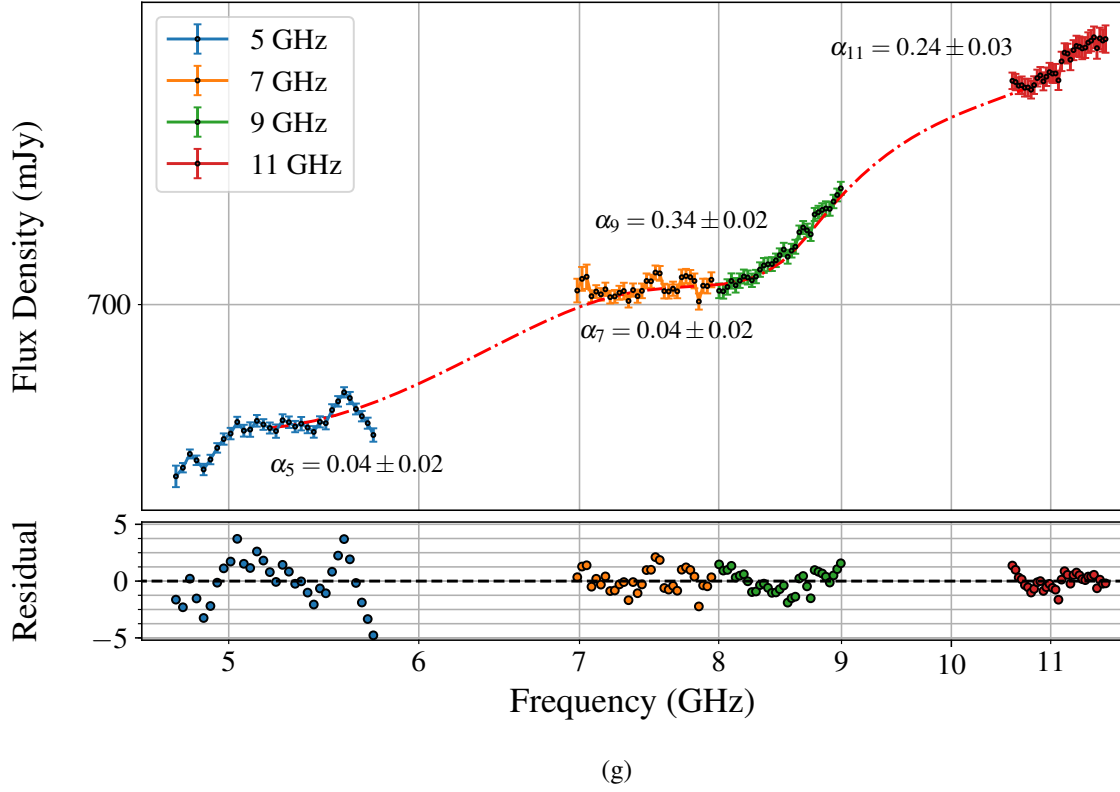


Figure 2. Resolved SEDs and residuals of spectral fitting of TXS 0506+056 from 5-11 GHz for: (a) epoch 1, (b) epoch 2, (c) epoch 3, (d) epoch 4, (e) epoch 5, (f) epoch 6, and (g) epoch 7. The spectral index values for each base-band are displayed on the plots as α_ν . **Note:** The red dash-dot lines are cubic spline interpolations, and are included to guide the eye to the general trend of the SED. They do not represent any fitting to the data. Residuals were calculated from the spectral index fitting model (see Eq. 4), not from the cubic interpolation.

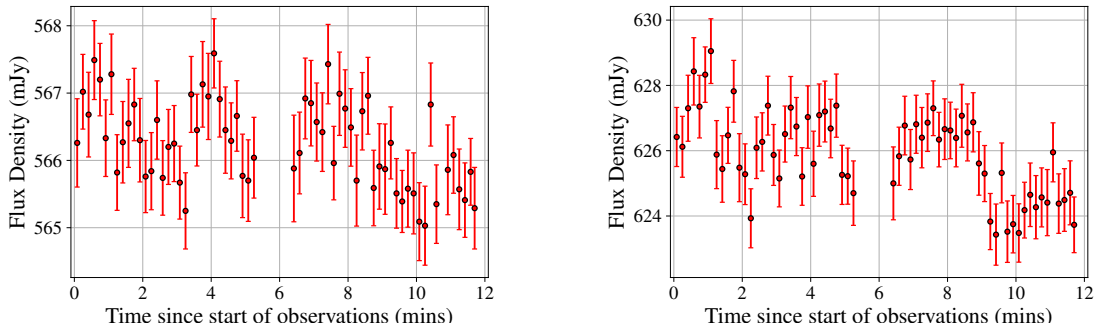


Figure 3. Resolved light curves of TXS 0506+056 during epoch 1 observation in the 5 GHz base-band (*left*), and 7 GHz base-band (*right*).

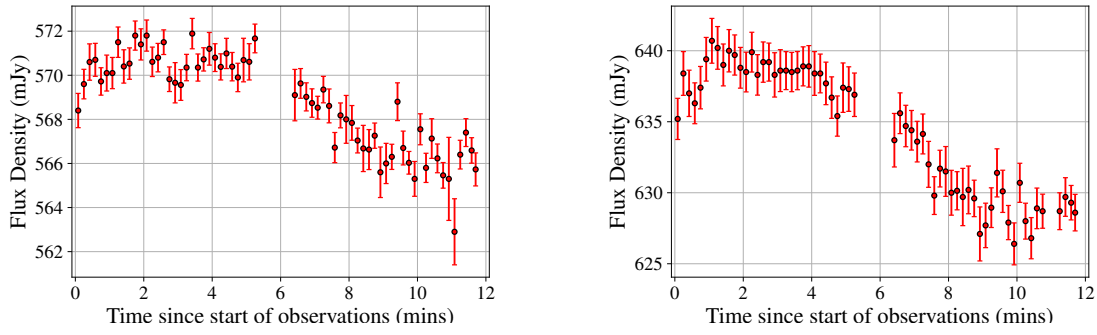


Figure 4. Resolved light curves of TXS 0506+056 during epoch 2 observation in the 5 GHz base-band (*left*), and 7 GHz base-band (*right*). We can clearly see both light curves follow a similar pattern.

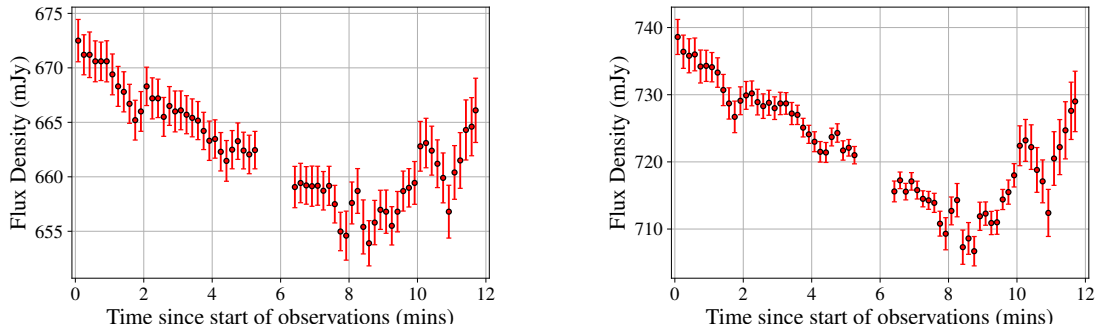


Figure 5. Resolved light curves of TXS 0506+056 during epoch 2 observation in the 9 GHz base-band (*left*), and 11 GHz base-band (*right*). A steadily decreasing flux density, followed by a sharp peak, potentially from a small flare, is clearly identifiable in both light curves.

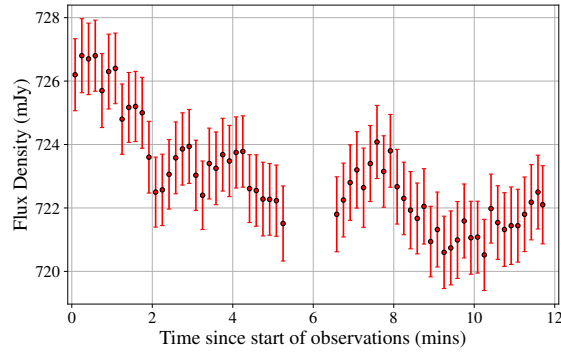


Figure 6. Resolved light curves of TXS 0506+056 during epoch 4 observation in the 11 GHz base-band. This was the only frequency that showed significant variability during this observation.

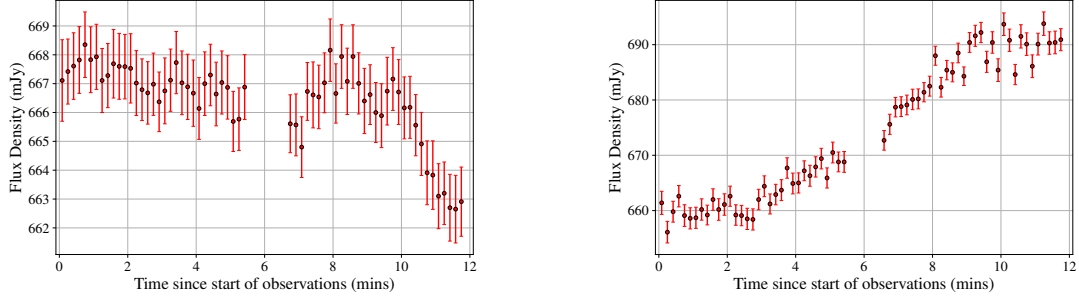


Figure 7. Resolved light curves of TXS 0506+056 during epoch 7 observation in the 5 GHz base-band (*left*), and 7 GHz base-band (*right*).

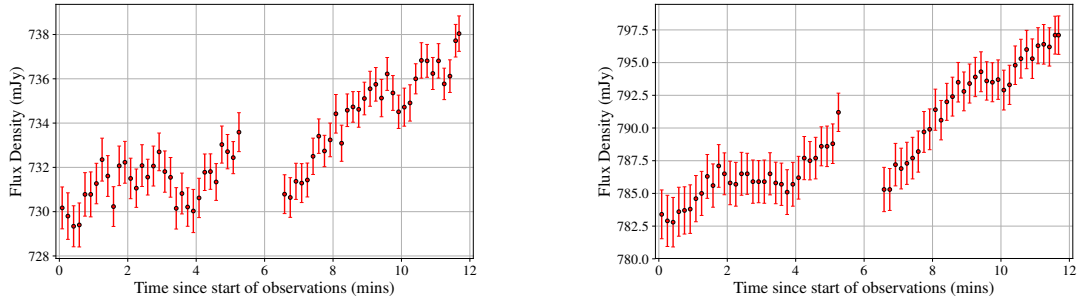


Figure 8. Resolved light curves of TXS 0506+056 during epoch 7 observation in the 9 GHz base-band (*left*), and 11 GHz base-band (*right*). A steadily decreasing flux density, followed by a sharp peak, potentially from a small flare, is clearly identifiable in both light curves.

4. DISCUSSION

4.1. Flux Calibration

An important note and should be made in regards to the flux calibrator used for the duration of the VLA observations, 3C138. [Perley & Butler \(2017\)](#) reviewed the flux-density scale with recent VLA observations and determined 3C138 has significant flux density variations (5% – 16% lower than in 2012, declining over all frequencies), and is not recommended as a flux density calibrator. The standard used in this project was the “Perley–Butler 2013”, so it is possible that the flux density scaling of the data is incorrect.

The variability of 3C138 may also be a cause of the inconsistency seen in the SEDs at 8 GHz for epochs 2 and 6. The flux scale was calibrated separately for each base-band; the 7 GHz data used the C band model of the Perley–Butler standard, while the 9 GHz used the X band model. If the source has experienced a change in flux density between the two bands, then we might expect a discrepancy between the flux scales used to calibrate the data. If 3C138 is experiencing any short term variability as well, then the error in flux scale could differ from observation to observation.

4.2. Evolution of Spectral Index

TXS 0506+056 clearly has a flat radio spectrum ($\alpha \leq 0.5$) from 5 – 11 GHz, which is a well known property of blazars ([Kimball & Izevic 2008](#)). Examining Figure 2, (a) – (g), we observe a general trend in most base-bands (specifically epochs 1 (a), 2 (b), 4 (d), 6(f) and 7(g)) of a flatter

index ($0.02 \leq \alpha \leq 0.15$) at 5 GHz. The spectral index then steepens from 5 to 7 GHz in epochs 1, 2, 3, and 4 to $0.33 \leq \alpha \leq 0.47$, flattening out again at 11 GHz. This shape of SED appears most consistent with the jet emission model of [Pe’er & Casella \(2009\)](#), in which electrons are accelerated once at the base of the jet, and experience non-replenishing adiabatic losses. Other models studied in this work (and other works, for example see [Abdo et al. 2010](#), for a review of FERMI bright blazar SEDs), which exclude adiabatic losses, result in an SED with a uniform spectral index in the low-frequency radio regime. The slight variations in the SED from observation to observation could be explained by the magnetic field of the jet varying. [Pe’er & Casella \(2009\)](#) showed that the magnetic field influences that flux at radio frequencies in a nontrivial manner.

At 11 GHz, it appears that some of the SEDs could be reaching a peak flux density, with the spectral slope approaching 0, suggesting TXS 0506+056 is a low frequency peaked BL Lac object (LBL) ([Böttcher 2010](#)). A synchrotron peak around 10–12 GHz is consistent with many SEDs observed by [Abdo et al. \(2010\)](#) in their study of FERMI bright blazars, although it is impossible to determine if the SED is indeed peaking near this frequency without observations into the higher adjacent frequency bands.

Epoch 6 is an obvious outlier to the other observations. Instead of an increasing flux density with frequency, we see it decreasing. The 5 GHz average amplitude is usually around $580 \sim 600$ mJy, increasing to ~ 700 mJy at 11 GHz. For epoch 6, we see quite the opposite. The flux density is approximately at an average (although it shows significant variability, averaged over the base-band $\alpha = 0.02$) flux density of 690 mJy, decreasing to ~ 600 mJy at 11 GHz. [Pe’er & Casella \(2009\)](#) showed that a change in the geometry of the jet (with adiabatic losses modelled) can alter the shape of the SED significantly (see their Figure 10, for a quick overview).

It is unclear whether the large fluctuations seen in some observations (e.g. in epoch 6 and epoch 7 at 5 GHz) are real, or due to systematic/calibration errors. One would not expect to see any features, as BL Lacs are known to have featureless, non-thermal continuum emissions. No structures are seen to exist between observations, so external causes of the fluctuations can likely be ruled out. The study of blazar spectra down to this size of frequency bin appears to be a relatively untouched subject, and much future research is needed before any definitive conclusion can be drawn from these results.

4.3. Variability in TXS 0506+056

The % rms and χ^2 values in these epochs for epochs 3, 4, 5 and 6 suggest the jet was relatively stable during these periods. The 11 GHz base-band in epoch 4 does show some variability (Figure 6); we see the flux density decreasing over the observation. If we consider the flux density values in Table 3, we can see that the flux density continually increases over these three epochs however. While no short term variability is observed in these epochs, it was clearly in some sort of multi-day flaring state from 2017 October 09–24. This can also be clearly seen in the entire observation light curve in the top panel of Figure 1.

The lower 5 GHz and 7 GHz base-bands of epoch 1 indicate some variability in the spectrum. Looking at the light curves in Figure 3, the variability in epoch 1 appears to be quite random, with no immediately noticeable structure or relationship in the variability between the two low

frequency base-bands. It is difficult to say whether this is indicative of activity with the jet, or due to a systematic uncertainty. Significant variability was not observed in the high frequency base-bands in this epoch.

However, the epoch 2 light curves clearly show variability in all frequency bands, having some of the highest % rms and χ^2 values. Moreover, a clear structure can be identified in the light curve; a flux decrease is seen in the latter half of the 5 and 7 GHz windows (Figure 4), while a steady decrease is observed in the first 8 minutes at 9 and 11 GHz (Figure 5). A sharp peak and rise is seen at around 10 minutes of observation, tracking very similarly in both of the high bands. The clear and similar structure between the light curves suggest this variability is likely real, and not due to any systematic errors. The fact that this change in flux density is occurring on the scale of minutes could indicate activity in the jet. If we compare the 5 GHz to 7 GHz, at an initial glance, there appears to be no lag between the light curves of the base-bands (withing the rms limits). The same can be said about the 9 and 11 GHz curves. If a time lag in the variability exists within the bands, it is not detectable at this time resolution.

All base-bands showed significant variability in epoch 7 as well. The lower base-bands in Figure 7 do not show any immediate obvious connections in the structure of their variability. The variability does appear to be real however, as the curves are varying smoothly and trackable for most of the observation. At 7 GHz we see some scattering of data for the last ~ 1 minute of the observation. This is most likely an issue with self-calibration solutions of the flux density. An clear connection is seen in the high base-bands, as can be seen in Figure 8. It appears as if a small flare may be occurring at around the 6 minute mark of the observation, with an overall increase of flux density is observed.

We cannot connect the C band variability to the X band variability in any case. In order to determine if the type of variability, and hence the cause, is shared between the bands, longer observations on target could reveal more details about the nature of the variability.

The variability observed in TXS 0506+056 indicate it was likely in some form of active state following the IceCube neutrino detection, suggesting that there could be a connection between jet activity and the generation of these VHE astrophysical neutrinos.

5. CONCLUSION

The blazar TXS 0506+056 was observed with the VLA over 7 epochs following an IceCube astrophysical neutrino detection. Observations were completed in the C and X bands in VLA B (epochs 1 – 6) and A (epoch 7) configurations. The source was imaged with the CASA package and analyzed in a variety of ways: SEDs were created by sub-band (dividing each base-band into 32 windows of $\Delta\nu = 32$ MHz), and light curves were created over all epochs, as well as dividing each epoch into 10 second intervals.

The spectral index of TXS 0506+056 is generally consistent with the single acceleration, synchrotron and adiabatic heat loss model described by Pe’er & Casella (2009); we see a flat slope ($\alpha < 0.2$ in most cases) at lower frequencies, steepening (typically to $\alpha \sim 0.4$) between 7 – 9GHz, and flattening again near 11 GHz. A negative spectral index was observed for epoch 6. This could be explained by decrease in the jets magnetic field strength, or a change in the structure of the jet

itself (Pe'er & Casella 2009). It appears that adiabatic losses could play an important role in the emission processes of astrophysical jets.

Variability metrics were performed on the light curves for each base-band. Variability based on a χ^2 test showed the blazar was stable from 2017 October 09–24 on the time scale of the observation. Averaged over the span of these epochs however, we see an increase of flux density in all bands. The remaining epochs showed variability over the 11 minute observation. This could indicate that TSX 0506+056 is indeed in a state of heightened activity. Whether or not this activity is linked to the IceCube detection of an astrophysical neutrino cannot be definitively answered at this point. Further research down to this spectral resolution, and longer observations of a suspected neutrino counterpart is needed.

REFERENCES

- Abdo, A.A., Ackermann, M., Aguero, I., et al., 2010, *ApJ*, 716:30
- Atoyan, A., Dermer, C.D. 2003, *ApJ*, 586:79
- Biermann, P.L., Strittmatter, P.A., *ApJ*, 322:643-649
- Blandford, R.D., Königl, A., 1979, *ApJ*, 232:34
- Böttcher, M. 2012, *Fermi Meets Jansky - AGN at Radio and Gamma-Rays*, p.41
- CASA Cookbook and User Reference Manual, 2010, <https://CASA.nrao.edu/Release3.4.0/docs/userman/UserMansu259.html>, last visited: April, 2018
- Clark, B.G. 1980, *Astron. & Astrophys.*, 89:377
- Dermer, C.D., 2007 *J. Phys.: Conf. Ser.* 60 8
- Fossati, G., Maraschi, L., Celotti, A., et. al., 1998, *MNRAS* 199,433
- Ghisellini, G., Celotti, A., Costamante, L., 2002, *Astron. Astrophys.* 386, 3, 833
- Gupta, A.C., Agarwal, A., Bhagwan, J. 2016, *MNRAS*, 458,1127
- Halzen, F. 2016, *Nature Physics*, 13, 232
- Hughes, P.A., Aller, M.F., Aller, D.H 2011 *MNRAS*, 735,2
- IceCube Collaboration, 2013, *Science*, 342, 1242856
- IceCube Collaboration, 2018, *Embargoed*, submitted
- Kimball, A., Izevic, Z., 2008 *AJ*, 136, 684
- Madejski, G., Sikora, M., 2016, *ARA&A*, 54:725
- Marscher, A.P. 2009, *ArXiv:0909.2576*, *Lect. Notes Phys.* 794
- Marscher, A.P. 2014, *ApJ*, 780:87
- Mészáros, P. 2017, *Annual Review of Nuclear and Particle Science*, Vol. 67:45-67
- Murase, K., Inoue, Y., Dermer, C.D. 2014 *Phys. Rev. D* 90, 023007
- O’Riordan, M., Pe’er, A. Mckinney, J.C. 2017, *ApJ*, 843,2:81
- Pe’er, A., Casella, P. 2009, *ApJ*, 699:1919
- Perley, R.A., Butler, B.J., 2017, *ApJS.S.*, 230:7
- Urry, M., 2012, *Astronomical Review*, 7, 2
- Urry, M., Padovani, P., 1995, *Publications of the Astronomical Society of the Pacific*, 107: 803
- Waxman, E., Bahcall, J., *Phys. Rev. D* 59, 023002